Small Structures

www.small-structures.com

RESEARCH ARTICLE OPEN ACCESS

Water-Repellent, Surface-Adaptive, and Switchable Adhesive Patch Using Microstructured Shape Memory Polymers

Jaeil Kim | Geonjun Choi | Seongjin Park | Jong Woo Han | Hyung Wook Park | Hoon Eui Jeong

Department of Mechanical Engineering, Ulsan National Institute of Science and Technology (UNIST), Ulsan, Republic of Korea

Correspondence: Hoon Eui Jeong (hoonejeong@unist.ac.kr)

Received: 1 September 2025 | **Revised:** 19 November 2025 | **Accepted:** 14 December 2025

Keywords: adhesion | shape memory polymer | stiffness variable polymer | superhydrophobicity | water repellency

ABSTRACT

Strong yet switchable adhesion in wet environments remains a critical challenge for applications spanning underwater robotics, biointerfaces, and adaptive gripping systems. Conventional wet adhesives suffer from limited surface adaptability, loss of adhesion due to interfacial water, and poor controllability. Here, we report a multifunctional adhesive patch that integrates superhydrophobic micropillar arrays with a thermoresponsive shape memory polymer (SMP) matrix to simultaneously achieve water-shedding capability, robust underwater adhesion, and thermally programmable detachment. The micropillar geometry repels interfacial water and establishes a dry contact, while the SMP matrix dynamically tunes modulus and contact geometry through reversible glassy–rubbery transitions, enabling conformal adaptation and recovery-driven detachment. As a result, the patch demonstrates exceptional underwater pull-off strength (612.5 kPa), a high switching ratio ($F_{\mathrm{on}}/F_{\mathrm{off}} = 46.3$), and excellent durability over 500 cycles. Furthermore, when integrated into a thermally controlled robotic gripper, the patch successfully performs submerged pick-and-place operations on rough and irregular substrates, highlighting its potential for next-generation underwater manipulation, soft robotics, and smart biomedical adhesives.

1 | Introduction

Reliable adhesion in wet environments is critically needed in applications such as wound dressings [1–4], skin-mounted electronics [5–7], and underwater object transportation [8, 9], where interfacial water obstructs intimate solid–solid contact. Achieving strong wet adhesion is particularly challenging because the interfacial liquid disrupts contact formation while target substrates exhibit large variations in roughness and surface chemistry [10, 11]. Moreover, emerging fields in underwater robotics, biointegrated devices, and medical tools increasingly demand adhesives that combine strong underwater adhesion with conformability, reusability, and actively controllable switching [12, 13].

Chemical wet adhesives based on catechol chemistry, ionic networks, and supramolecular interactions have shown strong underwater bonding through molecular-level interactions [14–16]. However, these bonds are difficult to reverse, limiting their usefulness in systems requiring controlled or repeated detachment [17]. Hydrogel adhesives offer softness and biocompatibility, yet their hydrophilicity and limited microscale adaptability often result in incomplete interfacial contact and poor adhesion on rough wet substrates [18–23].

Bio-inspired superhydrophobic micropillar adhesives offer an alternative strategy in which trapped air pockets repel interfacial water and promote dry contact formation [24–29]. These structured adhesives demonstrate good repeatability and moderate adaptability to rough surfaces [30–32], but they still suffer from low underwater adhesion strength due to an intrinsic geometric trade-off: maintaining water repellency requires a low solid

---

Jaeil Kim and Geonjun Choi contributed equally to this work.

fraction, whereas generating strong adhesion requires a high real contact area [25]. This incompatibility has made it difficult for conventional microstructured adhesives to simultaneously achieve robust water repellency and strong wet adhesion.

Shape-memory-polymer (SMP) adhesives provide a complementary route by switching modulus across the transition temperature (T_m) to enhance interfacial contact [33–38]. Their shape-fixing and recovery capabilities enable reversible adhesion, but previously reported SMP-based adhesives still exhibit several limitations, especially under wet conditions. For example, prior bulk SMP systems rely on pressure-driven liquid squeeze-out and therefore require large preloads and prolonged heating at elevated temperatures to remove interfacial water, conditions that narrow the practical underwater operating window [39]. Other SMP designs achieve reversible adhesion in dry environments through embedding or localized tip deformation [40, 41], but these mechanisms lack active water-removal capability and thus are ineffective for robust adhesion on submerged substrates. Overall, existing microstructured and SMP-based adhesives do not resolve the inherent conflict between sustaining water repellency and forming a large real contact area, and therefore cannot simultaneously deliver strong wet adhesion, reliable switching, and broad substrate adaptability.

Here, we present a microstructured shape-memory polymer (MSMP) patch that overcomes these limitations by integrating a superhydrophobic micropillar architecture with a thermally tunable SMP matrix. Upon initial contact, the microstructures repel and expel interfacial water to establish a dry interface even under a gentle preload. When heated above T_m, the softened SMP enables deep geometric adaptation of the pillars, generating an ultralarge real contact area for exceptionally strong wet adhesion. Cooling fixes this adapted geometry, while reheating triggers shape recovery and sharply reduces the contact area, enabling reliable and actively controllable switching. Through this integrated materials–geometry mechanism, the MSMP patch achieves high underwater pull-off strength (612.5 kPa), large switching ratio (46.3), excellent durability (>500 cycles), and robust adhesion across substrates of varying roughness. Its practical utility is further demonstrated in a submerged robotic gripping system capable of reliable pick–transport–place operations on diverse objects.

2 | Results and Discussion

2.1 | Design and Fabrication of the Microstructured SMP Patch

Figure 1 depicts a conceptual schematic of the water-repellent, surface-adaptive, and reversible MSMP patch proposed in this study. The patch design aims to incorporate multifunctional attributes, including water repellency, strong adhesion under wet conditions, and on-demand adhesion switchability (Figure 1a-i). To realize these functionalities, a micropillar-based adhesive patch was fabricated using an SMP blend as the primary material (Figure 1a-ii,iii). The micropillar arrays provide key structural advantages, offering exceptional water repellency due to their low solid-fraction geometry. However, the micropillar array alone exhibits limited interfacial adhesion to various surfaces due to its reduced effective contact area. To address this limitation, we utilized an SMP blend as the main matrix of the adhesive patch [42]. The integration of the micropillar pattern with the SMP blend enables strong wet adhesion by combining water-repellent capability with temperature-dependent deformation and contact-area regulation. In addition, the shape-recovery characteristic of the SMP allows the contact area to decrease again, enabling reversible adhesion.

The SMP blend is composed of physically mixed polycaprolactone (PCL) and polyurethane acrylate (PUA). PCL acts as the switching segment owing to its crystalline melting behavior, while PUA serves as the permanent elastic matrix. This PCL/PUA combination offers complementary properties, with each component compensating for the limitations of the other. PCL provides stiffness tunability and shape-fixation capability, but its relatively low stiffness in the rubbery state restricts shape recovery [43]. In contrast, PUA exhibits high elasticity and recovery stress, enabling effective shape restoration [44].

Figure 1b illustrates the detailed adhesive mechanism of the MSMP patch. Upon approaching the substrate, the patch repels water and establishes a dry contact interface due to the superhydrophobic micropillar geometry. When heated above the T_m of the PCL/PUA blend, the material transitions to a rubbery state, softening the micropillars and allowing conformal contact under applied pressure. Subsequent cooling below T_m induces recrystallization and shape fixation, increasing the rigidity of the adhesive and maintaining high adhesion strength even under wet conditions. Interfacial adhesion ($F \propto \sqrt{G_c A E}$) is governed by both contact area (A) and mechanical modulus (E), with a given bonding strength (G_c) [45]. Upon reheating, the SMP effect allows the micropillars to recover their original geometry, reducing the contact area and enabling easy detachment. During this process, PUA contributes high elasticity and recovery stress, facilitating effective shape recovery. This reversible mechanism enables the adhesive to switch between strong adhesion ("on") and weak adhesion ("off") depending on the thermal condition.

Figure 1c presents the schematic fabrication process of the MSMP patch. The process begins with the preparation of a master mold with an array of negative micropillar patterns created by photolithography. The mold is then treated with a silane agent to facilitate clean demolding. Subsequently, the PCL/PUA blend presolution is prepared by dissolving both polymers (10 wt%) in dimethylformamide (DMF) and stirring for 24 h for complete homogeneity. The presolution is then drop-casted onto the master mold, UV-cured, and demolded. Figure 1d shows scanning electron microscope (SEM) images of the fabricated microstructured PCL/PUA adhesives, exhibiting uniform micropillar structures with a diameter of 15 μm and height of 15 μm.

2.2 | Thermomechanical Properties and Surface Adaptability of MSMP Patch

Figure 2 characterizes the thermomechanical properties and reversible surface adaptability of the MSMP patch. To enable efficient adhesion switching, the SMP must maintain sufficiently low stiffness in the rubbery state for conformal contact, while ensuring high modulus and reliable shape fixation in the glassy state. Moreover, the rubbery-state modulus should be finely tuned to provide adequate recovery stress for detachment without sacrificing adaptability. Note that the recovery strength ($\sigma_{stress} \propto E_{rubbery} \times \varepsilon_{prestrain}$) mainly depends on the rubbery state

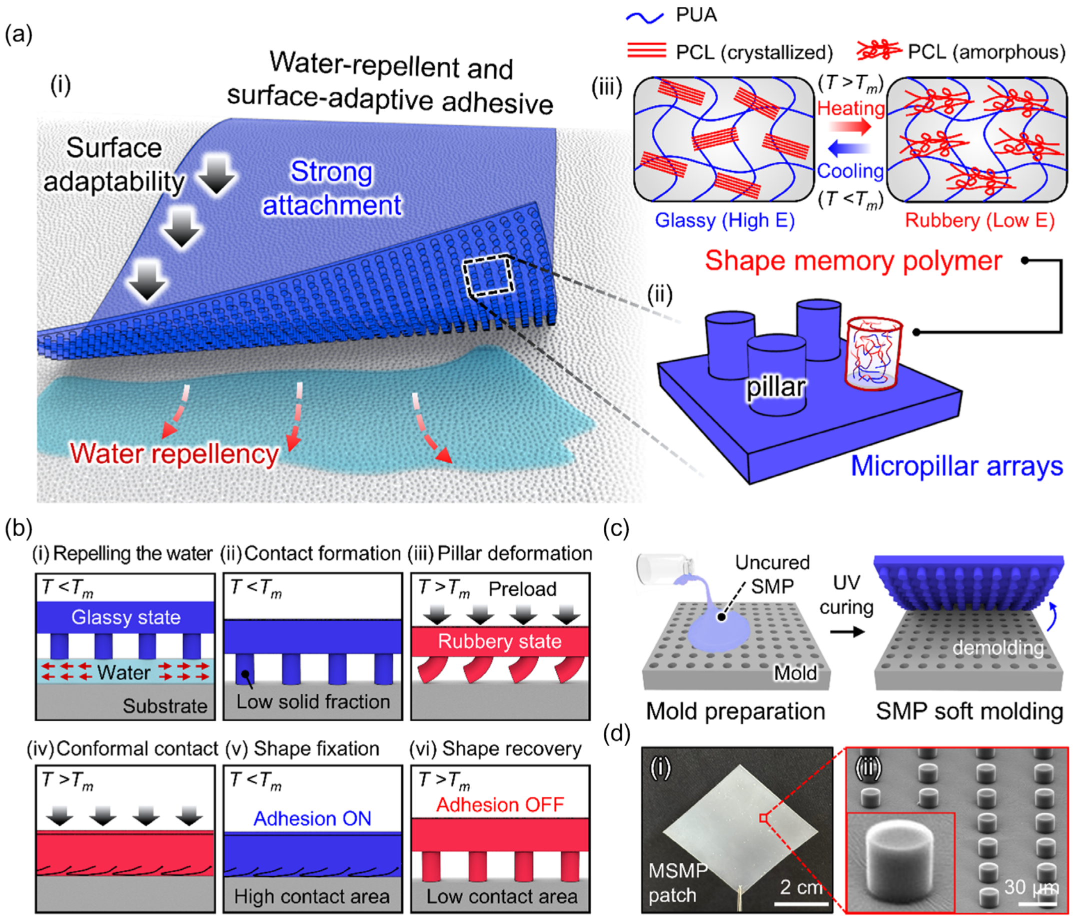

FIGURE 1 | Design, mechanism, and fabrication of the microstructured SMP patches. (a) Schematic illustration of the multifunctional MSMP patch: (i) overall concept combining water repellency, surface adaptability, strong wet adhesion, and thermal switchability, (ii) micropillar array that provides water shedding and dry contact formation, and (iii) thermally responsive SMP matrix exhibiting a reversible transition between glassy and rubbery states. (b) Sequential adhesion mechanism of the microstructured SMP adhesive patch on wet substrates. (c) Fabrication process of the adhesive patch using mold replication. (d) (i) Optical image of the fabricated patch. (ii) SEM image showing uniform micropillar structures (diameter = 15 μm, height = 15 μm).

modulus (E_{rubbery}), as the prestrain ($\varepsilon_{\text{prestrain}}$) is predetermined by the surface adaptation process [35, 46].

As shown in Figure 2a, the PCL/PUA SMP blends exhibit high G' below T_m (glassy state) and a sharp modulus drop above T_m (rubbery state) (Figure S1, Supporting Information). The glassy- and rubbery-state moduli can be systematically adjusted by controlling the PCL-to-PUA ratio. A higher PCL content increases glassy-state modulus by enhancing crystallinity and physical crosslinking, as confirmed by intensified diffraction peaks in X-ray diffraction (XRD) patterns (Figure S2, Supporting Information) [47]. Conversely, increasing the PUA content reinforces the rubbery-state modulus through its crosslinked elastic network, thereby enhancing recovery stress. Such tunable moduli enable the blends to effectively balance adaptability, adhesion strength, and detachment capability.

Figure 2b presents the differential scanning calorimetry (DSC) thermograms, confirming that all blends exhibit a melting transition near 58°C with minor variations attributed to crystallinity differences. The presence of a single endothermic peak for each blend indicates that PCL and PUA are miscible, forming a homogeneous phase without macroscopic phase separation [48]. Cyclic thermomechanical tests further evaluated the shape fixity ratio (R_f) and shape recovery ratio (R_r) (Figure 2c), which quantify the ability to retain a programmed shape after cooling and to restore the original shape upon reheating, respectively. Higher R_f and R_r values indicate superior shape retention and recovery performance. Among the tested compositions, the 1:1 PCL-to-PUA blend exhibited the most balanced performance, achieving R_f of 99.2% and R_r of 98.8%, and maintained these values after repeated cycles (Figure S3, Supporting Information).

Figure 2d demonstrates the exceptional surface adaptability of the MSMP patch using 3D laser confocal microscopy. The 1:1 PCL-to-PUA patch conformed to a rough sandpaper surface, exhibiting a surface profile nearly identical to the substrate, indicating intimate contact even on microscopically rough topography. The adapted geometry remained stable upon cooling, while reheating induced full recovery to the original micropillar configuration, confirming excellent thermally driven reversibility and shape-memory performance.

To enable rapid and repeatable self-detachment, the SMP must generate sufficient recovery stress to overcome the interfacial work of adhesion. Figure 2e quantitatively compares the storage modulus and recovery strength across compositions. As the PUA fraction increases, both rubbery-state modulus and recovery strength increase accordingly. Accordingly, Figure 2f demonstrates that the 1:1 blend produced sufficient recovery stress to fully restore

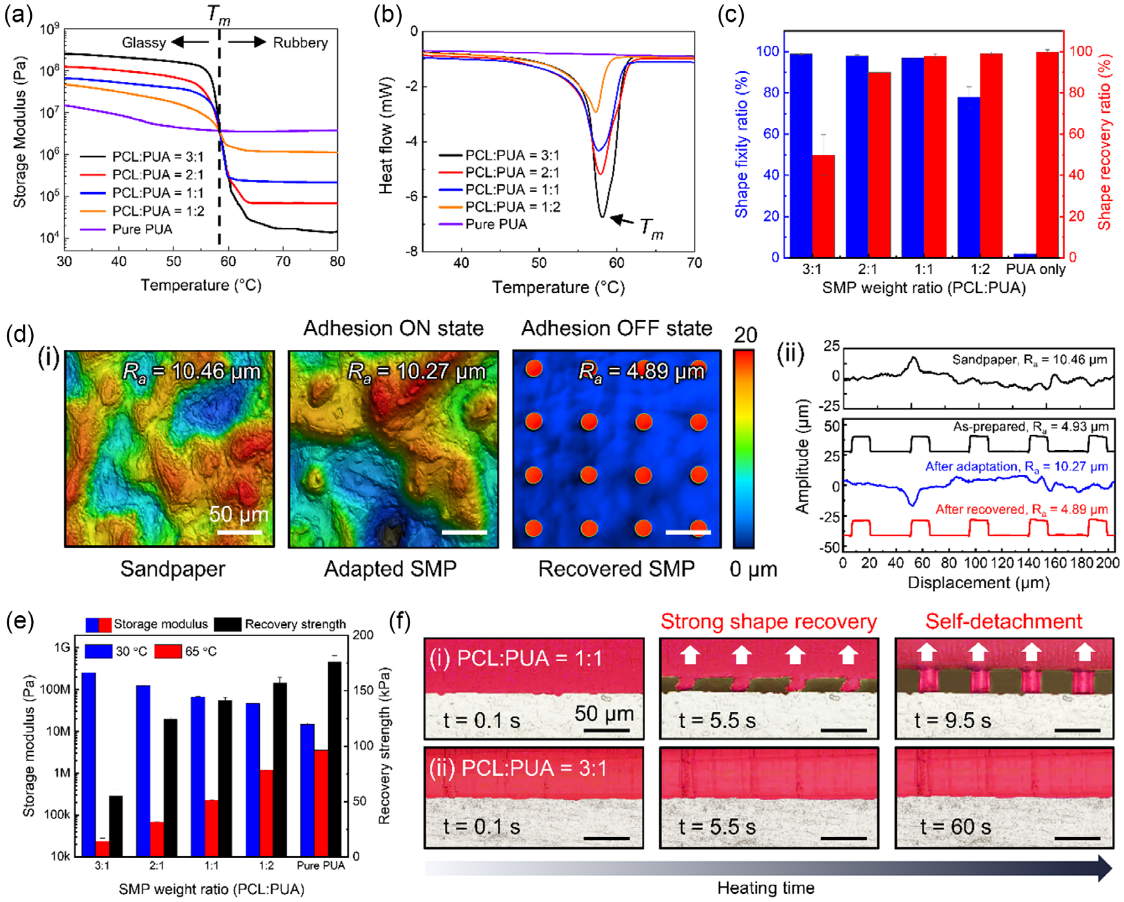

FIGURE 2 | Thermomechanical and surface adaptive behaviors of the MSMP patch. (a) Storage modulus (G') of SMP blends with varying PCL-to-PUA weight ratios measured over a range of temperatures. (b) DSC thermograms of SMP blends with varying PCL-to-PUA weight ratios. (c) Shape fixity ratio (R_f) and shape recovery ratio (R_r) of the blends evaluated by cyclic thermomechanical testing. (d) (i) 3D laser confocal microscope images and (ii) 2D cross-sectional profiles of sandpaper, adapted MSMP (adhesion ON state), and recovered MSMP (adhesion OFF state). (e) G'at 30°C and 65°C, and recovery strength of SMP blends with varying PCL-to-PUA weight ratios. (f) Sequential side-view images showing deformed (adhesion ON) and restored (adhesion OFF) configurations during shape recovery and self-detachment of SMP adhesives with (i) 1:1 and (ii) 3:1 PCL-to-PUA weight ratios.

its shape and detach within 9.5 s, whereas the 3:1 blend exhibited partial recovery and failed to detach due to insufficient recovery stress.

2.3 | Water-Repellent Behavior of MSMP Patch

The wetting and water-repellent properties of MSMP patches were characterized in Figure 3. Water contact angles (CAs) were measured for patches with different micropillar spacing ratios (SR) (Figures 3a and S4, Supporting Information). The planar surface exhibited a CA of 98°, indicating moderate hydrophobicity, whereas micropillar arrays with lower solid fraction showed substantially enhanced hydrophobicity: the CAs for SR 0.5, 1, 2, and 3 were 135.5°, 144.9°, 155.2°, and 160.5°, respectively. This enhancement is attributed to the increased trapped air fraction beneath the droplet, resulting in a stable composite interface consistent with the Cassie–Baxter model [49]. However, when the SR exceeded 4, the Cassie–Baxter state became unstable and transitioned to the Wenzel state, leading to reduced hydrophobicity [50]. The experimental CA values exhibited good agreement with theoretical predictions calculated using the Cassie–Baxter equation (Figure 3b) [51]:

$$\cos\theta = f_s(1+\cos\theta_Y) - 1 \tag{1}$$

where θ is the apparent contact angle, f_s is the solid fraction, and θ_Y is the intrinsic contact angle.

To further evaluate interfacial water repellency, we examined whether the patches could remove interfacial water upon contact with a wet substrate (Figure 3c). When the MSMP patch with SR 2 was gently brought into contact with a dyed-water droplet (10 μL) on glass, the micropillar array efficiently expelled the interfacial water and created a dry interface, while maintaining the Cassie–Baxter state even under light pressing (Figures 3c-i and S5 Supporting Information). Sequential optical images confirm minimal droplet residue, demonstrating strong water-shedding capability enabled by the micropillar geometry. After dry contact was established, additional pressing in the rubbery state allowed full conformal engagement via stiffness switching.

It should be emphasized that water removal and subsequent deformation occur in two distinct and sequential stages: (i) during the water-shedding stage, the micropillars remain rigid (glassy state) and do not collapse; (ii) deformation and conformal contact take place only after the interface becomes dry and the MSMP transitions into the rubbery state (Figure S6, Supporting

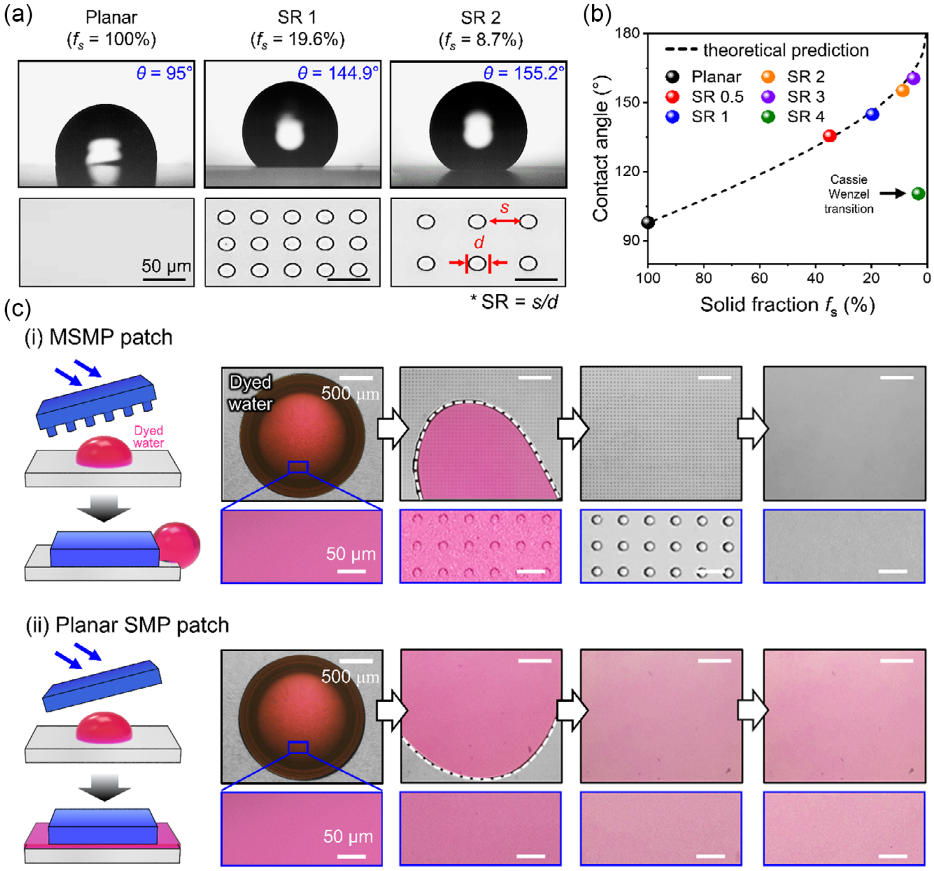

FIGURE 3 | Water-repellent behavior of the MSMP patch. (a) Photographs of water droplets on patches with varying spacing ratios (SR = s/d) and corresponding solid fractions (f_s), demonstrating increased hydrophobicity with decreasing f_s. (b) Comparison of experimentally measured CAs with theoretical predictions from the Cassie–Baxter model. (c) Schematics and optical microscopy images showing interfacial water removal on a glass substrate using (i) the MSMP patch, where the micropillar array actively expels the water droplet to form a dry interface, and (ii) the planar SMP patch, which fails to remove water and leaves a trapped liquid layer.

Information). By contrast, the planar SMP patch (Figure 3c-ii) failed to exclude the water droplet, resulting in a thin trapped water layer due to insufficient hydrophobicity and absence of microstructured air trapping. These results underscore the essential role of the micropillar array in facilitating interfacial water removal and enabling dry, conformal contact on wet substrates.

2.4 | Adhesion Performance of the MSMP Patch

To evaluate the strong adhesion and on-demand switching capability of the MSMP patch, pull-off adhesion tests were performed on glass substrates at 30°C (“on” state) and 65°C (“off” state) under wet conditions (Figure 4a). Among the tested samples, SR 2 was primarily used because its water-repellent microstructure enables stable dry contact formation, leading to reliable underwater adhesion. All adhesion measurements were conducted under a preload of 50 kPa, at which the pull-off force saturates, confirming full conformal contact at moderate pressure (Figure S7, Supporting Information). As a result, the MSMP patch achieved a maximum underwater pull-off capacity of 612.5 kPa and a switching ratio of 46.3, outperforming recently reported switchable wet adhesives (Figure 4b and Table S1, Supporting Information) [29, 52–60].

The thermally programmable adhesion operates through reversible deformation and recovery of the SMP micropillars across T_m (Figure 1b). Because a dry interface is established before heating, heat dissipation to the surrounding water during heating is substantially suppressed, allowing the surface to reliably reach the rubbery state and form a fully conformal contact. Consequently, the ON-state adhesion remained nearly unchanged at water temperatures between 10°C and 25°C (Figures S8 and S9, Supporting Information). To simultaneously secure intimate contact for strong adhesion and sufficient recovery stress for efficient detachment, the PCL:PUA = 1:1 composition was selected, as it offers an optimal balance of low rubbery-state modulus for deformation and high recovery stress upon reheating, exhibiting the highest adhesion switching ratio among all tested compositions (Figures 2e and S10, Supporting Information). Switching kinetics further confirmed fast and reliable thermal switching behavior, with response times of approximately 28.5 s for activation and 9.5 s for detachment (Figure S11, Supporting Information).

Figure 4c shows the dependence of adhesion on the micropillar SR. As SR increased to 3, ON-state adhesion sharply increased due to enhanced hydrophobicity and more efficient water removal, whereas SR > 4 led to a Cassie-to-Wenzel transition and reduced adhesion. Furthermore, OFF-state adhesion increased at high SR because the sparsely spaced pillars lacked sufficient recovery energy for complete shape restoration. Consequently, SR 2 exhibits

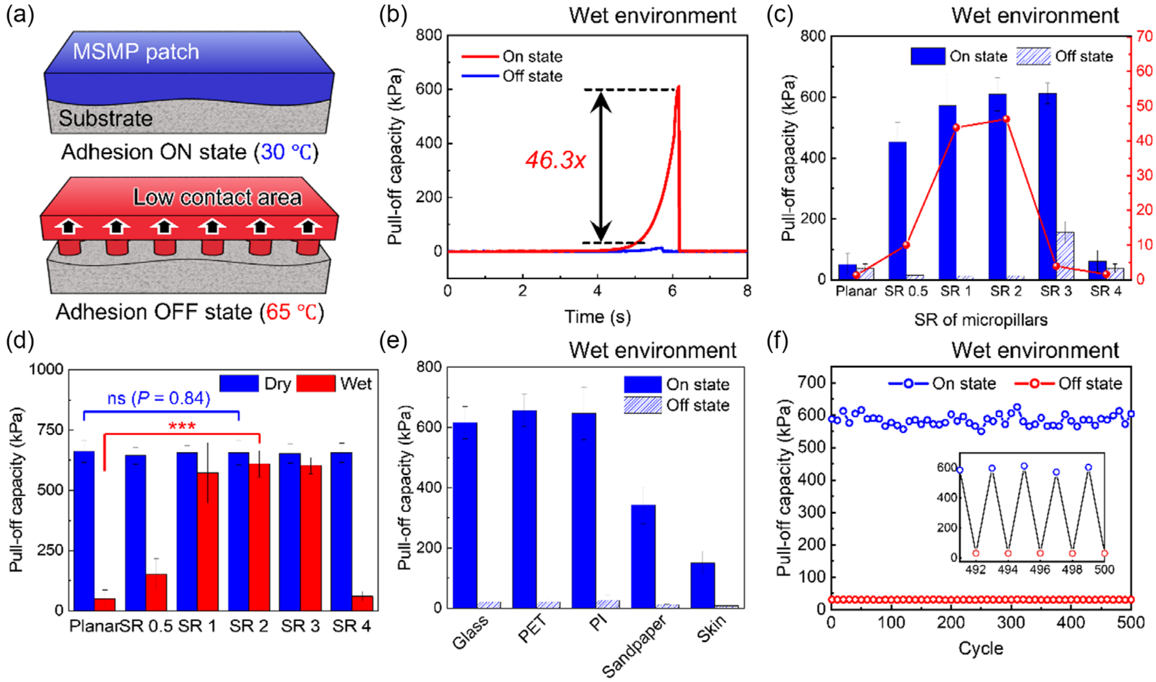

FIGURE 4 | Adhesion performance and switching characteristics of the MSMP patch. (a) Schematic illustration of the adhesion switching mechanism at low (30°C, “on” state) and high (65°C, “off” state) temperatures. (b) Representative pull-off capacity curves for the “on” and “off” states of the MSMP patch on a glass substrate under wet conditions. (c) Pull-off capacity and switching ratio as a function of the micropillar SR. (d) Pull-off capacity on glass substrates under dry and wet conditions for samples with varying SR. (e) Pull-off capacity on various substrates (glass, PET, PI, sandpaper, and porcine skin) under wet conditions. (f) Adhesion repeatability and durability of the patch over 500 attachment-detachment cycles. The pull-off capacity was obtained as the pull-off force divided by the nominal projected area of the patch. Statistical significance and *P* values were evaluated by unpaired Student’s *t*-test ($n = 5$; ns, not significant; $^{***}P < 0.001$).

the most balanced performance, combining high ON-state adhesion with low OFF-state adhesion. Adhesion remained stable across substrates with varying surface energies, except for extremely hydrophilic surfaces such as O_2-plasma–treated glass (Figure S12, Supporting Information).

Figure 4d demonstrates that SR 2 maintains consistently high ON-state adhesion in both dry and wet conditions, confirming that its underwater performance approaches its dry adhesion capacity. Figure 4e further highlights robust surface adaptability across substrates with distinctly different roughness levels (glass, PET, PI, sandpaper, and porcine skin), with negligible OFF-state adhesion maintained in all cases. Moreover, the MSMP patch preserved its adhesion strength and switching capability over 500 continuous adhesion–detachment cycles without degradation (Figure 4f), demonstrating excellent durability and reusability. Importantly, superhydrophobicity is only required during the initial water-removal step; once the MSMP conforms to the substrate and is fixed below T_m, the interface becomes dry and sealed, preventing moisture re-entry and eliminating the possibility of a Cassie-to-Wenzel transition. Consequently, prolonged submerged conditions do not compromise adhesion reliability, as confirmed by time-dependent adhesion measurements (Figure S13, Supporting Information) [61].

2.5 | Application of the MSMP Patch

To demonstrate the practical applicability of the MSMP patch, a robotic gripper with programmable adhesion was developed by integrating the SMP adhesive with a heating panel mounted on a robotic arm (Figure 5a). The heating panel, connected to an external power supply, generates heat via Joule heating through an embedded resistor, enabling precise thermal control for modulating the adhesion strength of the SMP adhesive. To ensure efficient heating in the underwater environment, the heater was encapsulated in a waterproof thermal insulation layer. As illustrated in Figure 5b, the adhesion state can be actively switched between strong attachment (“on” state) and easy detachment (“off” state) by controlling the temperature, thereby enabling repeatable underwater pick-and-place operations.

The force–displacement curves in Figure 5c indicate that the MSMP gripper generates a much higher underwater adhesion force (3.42 N) than the bare SMP pad, which exhibits only negligible adhesion (0.03 N). To quantitatively evaluate the response time of the gripper system, the normal load was recorded while the surface temperature of the MSMP was simultaneously monitored, allowing direct correlation of adhesion-switching behavior with the heating and cooling cycles (Figure 5d). After forming conformal contact and removing interfacial water, heating the MSMP above T_m, followed by cooling to 30°C, builds a stable underwater adhesive force within 28.5 s. Upon reheating, the adhesion is rapidly released within 9.5 s, demonstrating reliable and repeatable ON/OFF control of the gripping force.

The MSMP patch imparts critical capabilities to the robotic gripper system, including high adhesion under submerged conditions, secure attachment to substrates with varying surface roughness, and rapid on-demand detachment. Figure 5e further demonstrates the excellent surface adaptability of the MSMP patch-based gripper on substrates with a wide range of surface

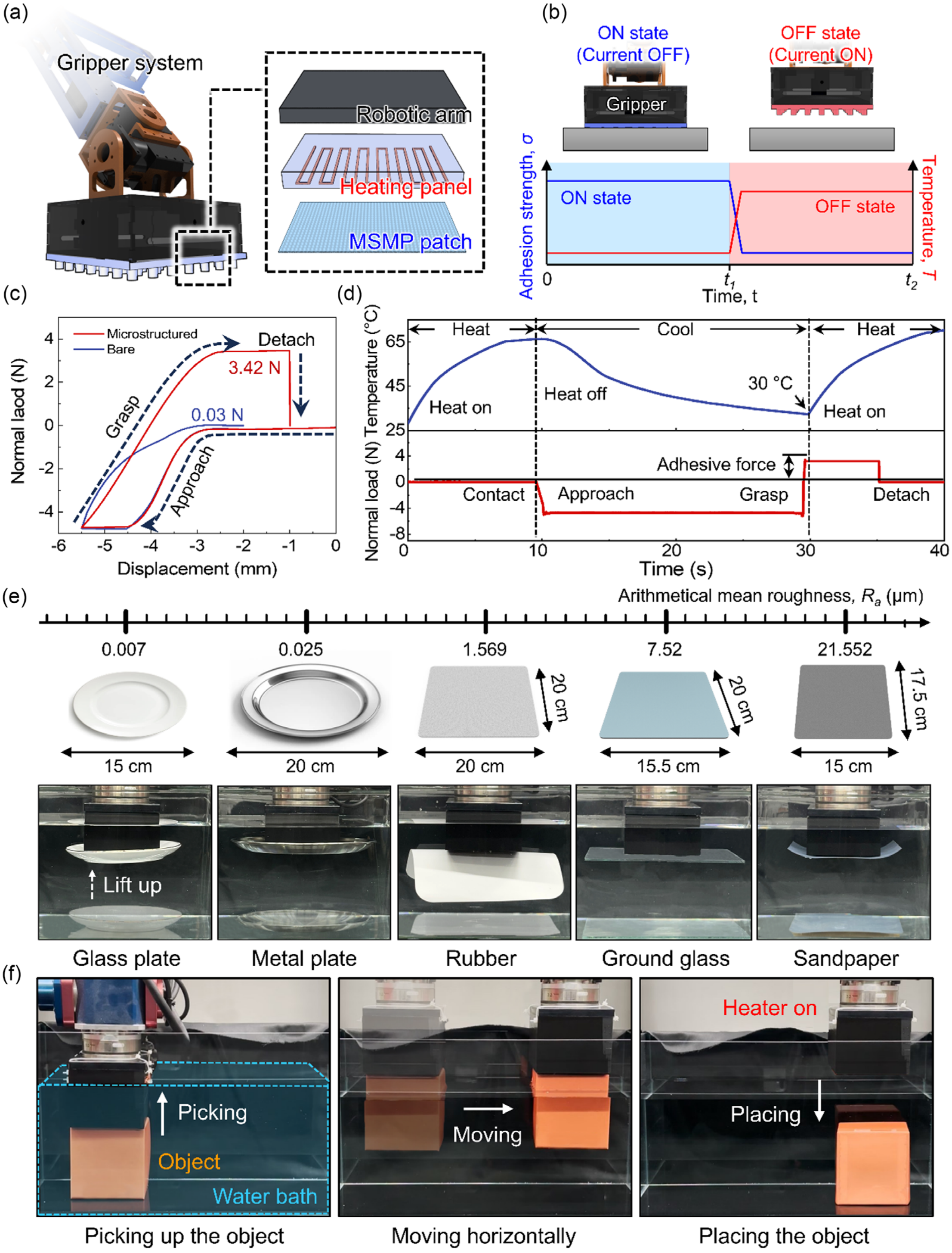

FIGURE 5 | Application of the MSMP patch. (a) Schematic of the robotic gripper system integrated with a heating panel and SMP adhesive. (b) Conceptual diagram of thermally switchable adhesion of the gripper system enabled by temperature modulation. (c) Force–displacement curves of the gripper system with and without microstructures against a ground glass. (d) Temperature-time and normal load-time curves for the ON and OFF states of the gripper system. (e) Demonstration of object lifting on substrates with various surface roughness (arithmetical mean roughness, $R_a = 0.007$–21.552 μm) under underwater conditions. (f) Sequential demonstration of pick–move–place operation using the SMP-based gripper.

roughness, from nanoscale to microscale features. To illustrate this capability, various objects with different roughness levels were selected, including a glass plate (arithmetical mean roughness, $R_a = 0.007$ μm), a metal plate ($R_a = 0.025$ μm), rubber ($R_a = 1.569$ μm), a ground glass plate ($R_a = 7.52$ μm), and sandpaper ($R_a = 21.552$ μm). The gripper system securely adhered to each target, demonstrating stable, slip-free gripping performance regardless of substrate roughness, and achieved a success rate above 92% across all tested substrates (Figure S14, Supporting Information).

Furthermore, to demonstrate underwater object delivery performance, the gripper system was evaluated for its ability to transport and place a cubic object accurately at user-defined positions (Figure 5f). The system continuously performed stable object picking, horizontal translation, and precise placement in sequence. These seamless operations were enabled by the MSMP patch's excellent surface adaptability, which allowed strong and conformal contact with the target surface and, upon reactivating the heating panel, induced rapid shape recovery that sharply reduced the contact area and adhesion strength, resulting in effortless and reliable self-detachment at the desired location. These results confirm that the MSMP patch-based gripper system provides programmable, reversible, and underwater-compatible adhesion switching, making it highly suitable for advanced robotic manipulation tasks under challenging submerged conditions [62–64].

3 | Conclusion

In summary, we developed a multifunctional MSMP patch that integrates strong wet adhesion, excellent surface adaptability, and thermally programmable adhesion switchability within a single platform. By combining water-shedding micropillar arrays with a thermoresponsive PCL/PUA SMP matrix, the patch overcomes the conventional trade-off between water repellency and wet adhesion. The micropillars enable dry contact formation by removing interfacial water, while the SMP matrix modulates mechanical stiffness and contact geometry in response to thermal stimuli, enabling both robust underwater adhesion and on-demand release.

This integrated design achieves high performance across multiple metrics, including superhydrophobicity (water CA of 155.2° at SR 2), large stiffness tunability (from 67.3 MPa at 30°C to 227.9 kPa at 65°C), and reliable shape-memory behavior. Consequently, the MSMP patch attains a pull-off strength of 612.5 kPa and a switching ratio of 46.3 under wet conditions, outperforming recently reported switchable wet adhesives [29, 52–60], while maintaining strong adhesion on PET, PI, sandpaper, and porcine skin. It also preserved stable performance over 500 adhesion–detachment cycles, confirming its durability and reusability.

To demonstrate real-world applicability, the MSMP patch was implemented in a thermally programmable robotic gripper equipped with an embedded heater. The gripper successfully performed precise, reversible, and repeatable pick-and-place operations underwater, even on rough substrates. These results highlight the MSMP patch's strong potential as a next-generation adhesive platform for underwater robotics, soft manipulation, and bio-interfacing devices that require robust yet controllable adhesion under challenging environments [65–67].

4 | Experimental Section

4.1 | Fabrication of Microstructured SMP Patches

First, the SMP blend was prepared by dissolving PCL ($M_n = 45\,000$, Sigma–Aldrich, USA) and PUA in N, N-dimethylformamide (DMF, Sigma–Aldrich, USA) at a total concentration of 10 wt%. The mixture was stirred at 60°C for 24 h to ensure complete dissolution and homogeneous blending. The PCL-to-PUA weight ratio was varied (3:1, 2:1, 1:1, 1:2, and pure PUA) to tune the thermomechanical properties of the resulting SMP. After mixing, the solution was degassed under vacuum to remove any entrapped air bubbles. The blend was then drop-cast onto a master mold with micropatterns. A polyethylene terephthalate (PET) film was placed over the cast solution, followed by ultraviolet (UV) curing for 2 min ($\lambda = 365$ nm, dose = 200 mJ cm^{-2}). After curing, the PET film was carefully peeled off, and the cured SMP adhesive was demolded from the Si mold.

4.2 | Thermomechanical Characterization

The thermomechanical properties of the SMP samples were characterized using a dynamic mechanical analyzer (DMA, Q800, TA Instruments, USA) operated in tension mode. Rectangular specimens (15 mm × 7 mm × 1 mm) were subjected to a sinusoidal strain of 0.2% at a frequency of 1 Hz, while the temperature was increased from 10°C to 70°C at a rate of 1°C min^{-1}. (DSC, Q2000, TA Instruments, USA) was performed to evaluate the thermal transitions of the SMP blends. Samples were heated from 10°C to 70°C at a rate of 5°C min^{-1} under a nitrogen atmosphere, and the melting temperature (T_m) was determined from the endothermic peak in the DSC thermogram.

4.3 | Shape Memory Characterization

The shape-memory performance was evaluated through cyclic thermomechanical testing using the same DMA system. Samples were heated to 65°C and elongated under a constant tensile load. The temporary shape was fixed by cooling the deformed samples to 30°C while maintaining strain, followed by unloading. During subsequent reheating, the recovery behavior was assessed in two modes: a stress-free mode to calculate the shape recovery ratio, and a fixed-strain mode to determine the recovery strength.

4.4 | Surface Characterizations

Surface morphologies of the MSMP patches were characterized using a field-emission scanning electron microscope (S-4800, Hitachi, Japan) after sputter-coating with a 5 nm Pt layer (K575X, Quorum Emitech, UK). Three-dimensional topography and surface roughness were analyzed using a laser scanning confocal microscope (VK-X3050, Keyence, Japan), and root mean square (RMS) roughness values were extracted from the surface maps using the VK-A3E software.

4.5 | Side-View Imaging of Shape-Recovery Behavior

Time-lapse side-view imaging of the MSMP micropillars was performed following the procedure. An MSMP patch (10 mm × 10 mm × 100 μm; PCL:PUA = 1:1 and 3:1) was first placed on a glass substrate for conformal adaptation. The lateral dimensions were chosen to be compatible with the working distance of the optical microscope used for side-view observation. To form the conformal, pillar-deformed (adhesion "on" state) geometry, the sample was heated using a heat gun (Bosch GHG20–63, Germany) until a thermocouple positioned adjacent to the patch reached 65°C. A normal preload of ~50 kPa was then applied using a stainless steel flat weight, inducing deformation of the micropillars and conformal contact. The preload was maintained as the sample cooled to 30°C, fixing the adapted geometry. For imaging, the entire patch–substrate assembly was mounted vertically on a chuck using double-sided tape so that the patch–substrate interface was exposed to the microscope. The mounted sample was reheated to 65°C using the same heat gun, during which the temperature-dependent shape-recovery process of the micropillars was captured in a time-lapse sequence. Imaging was performed on a representative central region of the patch.

4.6 | Wettability Analysis

CAs were measured using a contact angle goniometer (SDLAB 200TEZD, FemtoFab, Korea) by dispensing 5 μL deionized water droplets onto the sample surface under controlled conditions (25°C, 50% RH). The reported values represent the average of five measurements per sample.

4.7 | Adhesion Measurement

Pull-off adhesion tests were performed using a mechanical tester (Univert, Cellscale, Canada) equipped with a custom-designed fixture consisting of a substrate holder, a sample holder, and a vertically movable jig. Test substrates were fixed onto the lower holder using double-sided tape (3M, USA), and adhesive samples (1×1 cm^2) were similarly mounted on the upper holder with the adhesive surface facing downward. For wet adhesion measurements, the substrates were immersed in a small water bath placed on the sample holder. To initiate contact, a preload of 50 kPa was applied by placing calibrated weights on top of the sample holder. The holder was then connected to the movable jig using a fishing line, and the jig was retracted upward at a constant speed of 2 mm s^{-1} until detachment occurred, while the pull-off force was recorded. For "on" state adhesion, the samples were pressed against the substrates under a preload of 50 kPa at approximately 65°C (above T_m) using a heat gun (GHG 20–63, BOSCH, Germany), while the actual MSMP surface temperature was monitored using a type-K thermocouple and maintained within the rubbery-state regime (≈60–70°C). The adhered samples were then cooled to 30°C while maintaining the preload to fix the temporary shape. The "off" state adhesion was measured by reheating the samples to ≈65°C without applying additional preload prior to detachment, ensuring that only the glassy/rubbery transition governed the adhesion switching rather than precise temperature control (Figures S1 and S15, Supporting Information).

4.8 | Statistical Analysis

Datasets were analyzed using an unpaired Student's *t*-test for comparisons between two conditions. In all cases, *P* values less than 0.05 were considered statistically significant. Calculations were carried out using SPSS version 29.0.2.0. The means ± standard deviation for each dataset were calculated from at least five experiments.

Acknowledgments

J.K. and G.C. contributed equally to this work. This work was supported by National Research Foundation (NRF) of Korea (2021R1A2C3006297/2022R1A2C3007963).

Funding

This work was supported by the Ministry of Science and ICT, South Korea (2021R1A2C3006297/2022R1A2C3007963).

Conflicts of Interest

The authors declare no conflicts of interest.

Data Availability Statement

The data that support the findings of this study are available from the corresponding author upon reasonable request.

References

1. H. Guo, W. J. Zhang, Z. L. Jia, et al., "A Biodegradable Supramolecular Adhesive with Robust Instant Wet Adhesion for Urgent Hemostasis and Wound Repair," *Advanced Functional Materials* 34 (2024): 2401529.

2. M. T. Chen, Y. Wu, B. H. Chen, A. M. Tucker, A. Jagota, and S. Yang, "Fast, Strong, and Reversible Adhesives with Dynamic Covalent Bonds for Potential use in Wound Dressing," *Proceedings of the National Academy of Sciences of the United States of America* 119 (2022): e2203074119.

3. W. B. Zhao, W. T. Sun, W. J. Wang, Y. G. Zhang, and Q. M. Ma, "Robust and Wet Adhesive Self-Gelling Powders for Rapid Hemostasis and Efficient Wound Healing," *ACS Applied Materials & Interfaces* 16 (2024): 6756.

4. X. Peng, X. Xu, Y. R. Deng, et al., "Ultrafast Self-Gelling and Wet Adhesive Powder for Acute Hemostasis and Wound Healing," *Advanced Functional Materials* 31 (2021): 2102583.

5. J. Shin, B. Jeong, J. Kim, et al., "Sensitive Wearable Temperature Sensor with Seamless Monolithic Integration," *Advanced Materials* 32 (2020): 1905527.

6. F. Chen, Q. N. Zhuang, Y. C. Ding, et al., "Wet-Adaptive Electronic Skin," *Advanced Materials* 35 (2023): 2305630.

7. J. H. Cheng, J. Shang, S. J. Yang, J. B. Dou, X. H. Shi, and X. Y. Jiang, "Wet-Adhesive Elastomer for Liquid Metal-Based Conformal Epidermal Electronics," *Advanced Functional Materials* 32 (2022): 2200444.

8. C. H. Pang, J. K. Kim, Y. D. Wu, M. C. Yu, H. Y. Yu, and M. Sitti, "Bioinspired Microstructured Adhesives with Facile and Fast Switchability for Part Manipulation in Dry and Wet Conditions," *Advanced Functional Materials* 33 (2023): 2303116.

9. M. Li, W. J. Li, Q. W. Guan, et al., "A Tough Reversible Biomimetic Transparent Adhesive Tape with Pressure-Sensitive and Wet-Cleaning Properties," *ACS Nano* 15 (2021): 19194.

10. M. Kang, K. Sun, M. Seong, et al., "Applications of Bioinspired Reversible Dry and Wet Adhesives: A Review," *Frontiers in Mechanical Engineering* 7 (2021): 668262.

11. J. Li, A. D. Celiz, J. Yang, et al., "Tough Adhesives for Diverse Wet Surfaces," *Science* 357 (2017): 378.

12. Y. L. Zhang, S. H. Ma, B. Li, et al., "Gecko's Feet-Inspired Self-Peeling Switchable Dry/Wet Adhesive," *Chemistry of Materials* 33 (2021): 2785.

13. Z. Y. Liu and F. Yan, "Switchable Adhesion: On-Demand Bonding and Debonding," *Advanced Science* 9 (2022): 2200264.

14. L. Wistlich, A. Rücker, M. Schamel, A. C. Kübler, U. Gbureck, and J. Groll, "A Bone Glue with Sustained Adhesion under Wet Conditions," *Advanced Healthcare Materials* 6 (2017): 1600902.

15. B. D. B. Tiu, P. Delparastan, M. R. Ney, M. Gerst, and P. B. Messersmith, "Cooperativity of Catechols and Amines in High-Performance Dry/Wet Adhesives," *Angewandte Chemie International Edition* 59 (2020): 16616.

16. H. L. Yang, W. Q. Wang, C. J. Zhu, et al., “Reversible, Ultra-strong Underwater Adhesive based on Supramolecular Interaction for Instant Liquid Leakage Sealing and Robust Tissue Adhesion,” *Chemical Engineering Journal* 480 (2024): 148064.

17. B. Xue, J. Gu, L. Li, et al., “Hydrogel Tapes for Fault-tolerant Strong Wet Adhesion,” *Nature Communications* 12 (2021): 7156.

18. G. Y. Han, J. Y. Park, J. H. Back, M. B. Yi, and H. J. Kim, “Highly Resilient Noncovalently Associated Hydrogel Adhesives for Wound Sealing Patch,” *Advanced Healthcare Materials* 13 (2024): 2303342.

19. H. S. Liu, C. Liu, D. C. Shao, et al., “A Tough Janus Hydrogel Patch with Strong Wet Adhesion and Self-Debonding for Oral Ulcer Treatment,” *Chemistry Materials* 36 (2024): 4976.

20. X. D. Wang, Y. X. Guo, J. F. Li, et al., “Tough Wet Adhesion of Hydrogen-Bond-Based Hydrogel with On-Demand Debonding and Efficient Hemostasis ,” *ACS Applied Materials & Interfaces* 14 (2022): 36166.

21. H. Y. Yuen, H. P. Bei, and X. Zhao, “Underwater and Wet Adhesion Strategies for Hydrogels in Biomedical Applications,” *Chemical Engineering Journal* 431 (2022): 133372.

22. T. L. Wu, X. P. Zhang, Y. Liu, C. Y. Cui, Y. G. Sun, and W. G. Liu, “Wet Adhesive Hydrogel Cardiac Patch Loaded with Anti-oxidative, Autophagy-regulating Molecule Capsules and MSCs for Restoring Infarcted Myocardium,” *Bioactive Materials* 21 (2023): 20.

23. H. Zhou, Y. Fan, J. J. Huang, et al., “A Wet-Adhesive Hydrogel Patch with Rapid-Adhesion, Anti-Swelling, and Pro-Healing Properties for Sutureless Repair of Dural Tear,” *Advanced Healthcare Materials* 14 (2025): 2500761.

24. C. B. Dayan, S. Chun, N. Krishna-Subbaiah, D. M. Drotlef, M. B. Akolpoglu, and M. Sitti, “3D Printing of Elastomeric Bioinspired Complex Adhesive Microstructures,” *Advanced Materials* 33 (2021): 2103826.

25. V. Liimatainen, D. M. Drotlef, D. Son, and M. Sitti, “Liquid-Superrepellent Bioinspired Fibrillar Adhesives,” *Advanced Materials* 32 (2020): 2000497.

26. S. M. Kang, S. M. Kim, H. N. Kim, M. K. Kwak, D. H. Tahk, and K. Y. Suh, “Robust Superomniphobic Surfaces with Mushroom-like Micropillar Arrays,” *Soft Matter* 8 (2012): 8563.

27. Z. Y. Dai, S. Ding, M. Lei, et al., “A Superhydrophobic and Anti-corrosion Strain Sensor for Robust underwater Applications,” *Journal of Materials Chemistry A* 9 (2021): 15282.

28. T. I. Kim and K. Y. Suh, “Unidirectional Wetting and Spreading on Stooped Polymer Nanohairs,” *Soft Matter* 5 (2009): 4131.

29. S. Park, J. Kim, S. H. Lee, et al., “Water-repellent and Self-attachable Flexible Conductive Patch,” *Applied Physics Letters* 123 (2023): 071601.

30. S. Park, D. K. Kang, D. Lee, et al., “Multiscale Crack Trapping for Programmable Adhesives,” *Science Advances* 10 (2024): eadq3438.

31. H. E. Jeong, J. K. Lee, H. N. Kim, S. H. Moon, and K. Y. Suh, “A Nontransferring Dry Adhesive with Hierarchical Polymer Nanohairs,” *Proceedings of the National Academy of Sciences of the United States of America* 106 (2009): 5639.

32. J. Kim, G. Choi, S. Park, et al., “Smart Mechanical Structures and Design for Advanced Adhesives: A Review,” *International Journal of Precision Engineering and Manufacturing* 26 (2025): 757.

33. J. Eisenhaure and S. Kim, “An Internally Heated Shape Memory Polymer Dry Adhesive,” *Polymers* 6 (2014): 2274.

34. G. Choi, J. Kim, H. Kim, et al., “Motion-Adaptive Tessellated Skin Patches With Switchable Adhesion for Wearable Electronics,” *Advanced Materials* 37 (2025): 2412271.

35. C. Linghu, Y. C. Y. Liu, Y. Y. Tan, et al., “Overcoming the Adhesion Paradox and Switchability Conflict on Rough Surfaces with Shape-memory Polymers,” *Proceedings of the National Academy of Sciences of the United States of America* 120 (2023): e2221049120.

36. H. Meng and G. Q. Li, “A Review of Stimuli-responsive Shape Memory Polymer Composites,” *Polymer* 54 (2013): 2199.

37. X. F. Liu, L. Jia, Y. F. Li, et al., “Shape Memory Arrays Top Coated by Adjustable Mushroom with Switchable Adhesion to Both Solid and Liquid,” *Advanced Functional Materials* 34 (2024): 2312869.

38. A. Lendlein and S. Kelch, “Shape-Memory Polymers,” *Angewandte Chemie International Edition* 41 (2002): 2034,

39. J. K. Park, J. D. Eisenhaure, and S. Kim, “Reversible Underwater Dry Adhesion of a Shape Memory Polymer,” *Advanced Materials Interfaces* 6 (2019): 1801542.

40. C. L. Li, S. Zhang, J. Jiang, S. H. Wang, S. C. He, and J. Z. Song, “Laser-induced Adhesives with Excellent Adhesion Enhancement and Reduction Capabilities for Transfer Printing of Microchips,” *Science Advances* 10 (2024): eads9226.

41. C. H. Linghu, S. Zhang, C. J. Wang, et al., “Universal SMP Gripper with Massive and Selective Capabilities for Multiscaled, Arbitrarily Shaped Objects ,” *Science Advances* 6 (2020): eaay5120.

42. A. del Campo, C. Greiner, and E. Arzt, “Contact Shape Controls Adhesion of Bioinspired Fibrillar Surfaces,” *Langmuir* 23 (2007): 10235.

43. H. Zhang, H. T. Wang, W. Zhong, and Q. G. Du, “A Novel Type of Shape Memory Polymer Blend and The Shape Memory Mechanism,” *Polymer* 50 (2009): 1596.

44. L. Cao, X. F. Liu, H. Zhang, Z. B. Liu, L. Li, and J. P. Zheng, “3D Printable Dual-Cured PUA Elastomer Sensors: Low Viscosity, Volume Shrinkage, Heat Treatment Temperature and Excellent Mechanical Properties,” *Journal of Applied Polymer Science* 142 (2025): e57204.

45. M. D. Bartlett, S. W. Case, A. J. Kinloch, and D. A. Dillard, “Peel Tests for Quantifying Adhesion and Toughness: A review,” *Progress in Materials Science* 137 (2023): 101086.

46. Y. P. Liu, K. Gall, M. L. Dunn, and P. McCluskey, “Thermomechanics of Shape Memory Polymer Nanocomposites,” *Mechanics of Materials* 36 (2004): 929.

47. Y. C. Chien, W. T. Chuang, U. S. Jeng, and S. H. Hsu, “Preparation, Characterization, and Mechanism for Biodegradable and Biocompatible Polyurethane Shape Memory Elastomers,” *ACS Applied Materials & Interfaces* 9 (2017): 5419.

48. Y. S. Joo, J. R. Cha, and M. S. Gong, “Biodegradable shape-memory Polymers using Polycaprolactone and Isosorbide Based Polyurethane Blends,” *Materials Science and Engineering: C* 91 (2018): 426.

49. C. E. Cansoy, H. Y. Erbil, O. Akar, and T. Akin, “Effect of Pattern Size and Geometry on the use of Cassie–Baxter Equation for Superhydrophobic Surfaces,” *Colloids and Surfaces A: Physicochemical and Engineering Aspects* 386 (2011): 116.

50. N. A. Patankar, “Transition between Superhydrophobic States on Rough Surfaces ,” *Langmuir* 20 (2004): 7097.

51. E. Bormashenko, “Why does the Cassie–Baxter Equation Apply?,” *Colloids and Surfaces A: Physicochemical and Engineering Aspects* 324 (2008): 47.

52. J. Hwang, D. Lim, G. Lee, et al., “Ambient Air-operated Thermo-switchable Adhesion of N-isopropylacrylamide-Incorporated Pressure Sensitive Adhesives,” *Materials Horizons* 10 (2023): 2013.

53. L. Xiao, Z. Wang, Y. Sun, et al., “An Artificial Phase-Transitional Underwater Bioglue with Robust and Switchable Adhesion Performance,” *Angewandte Chemie International Edition* 61 (2022): 12189.

54. B. Zhang, L. H. Jia, J. R. Jiang, S. S. Wu, T. Xiang, and S. B. Zhou, “Biomimetic Microstructured Hydrogels with Thermal-Triggered

Switchable Underwater Adhesion and Stable Antiswelling Property," *ACS Applied Materials & Interfaces* 13 (2021): 36574.

55. A. Eklund, O. Ikkala, and H. Zhang, "Highly Efficient Switchable Underwater Adhesion in Channeled Hydrogel Networks," *Advanced Functional Materials* 34 (2024): 2214091.

56. S. Yang, Y. Ma, C. Qin, et al., Light-controlled Switchable underwater Adhesive," *SmartMat* 5 (2023): e1235.

57. H. Lee, D. S. Um, Y. Lee, S. Lim, H. J. Kim, and H. Ko, "Octopus-Inspired Smart Adhesive Pads for Transfer Printing of Semiconducting Nanomembranes," *Advanced Materials* 28 (2016): 7457.

58. S. C. Huang, Y. J. Zhu, X. Y. Huang, X. X. Xia, and Z. G. Qian, "Programmable Adhesion and Morphing of Protein Hydrogels for Underwater Robots," *Nature Communications* 15 (2024): 195.

59. Z. Wang, L. F. Guo, H. Y. Xiao, H. Cong, and S. T. Wang, "A Reversible underwater Glue Based on Photo- and Thermo-responsive Dynamic Covalent Bonds," *Materials Horizons* 7 (2020): 282.

60. C. Wu, Y. Cheng, K. Wang, et al., "Temperature-Mediated Controllable Adhesive Hydrogels with Remarkable Wet Adhesion Properties Based on Dynamic Interchain Interactions," *Advanced Functional Materials* 35 (2025): 2423099.

61. X. F. Wang, Y. C. Y. Liu, H. Y. Cheng, and X. P. Ouyang, "Surface Wettability for Skin-Interfaced Sensors and Devices," *Advanced Functional Materials* 32 (2022): 2200260.

62. M. Bruno, L. Portaluri, M. De Vittorio, S. Gorb, and M. Scaraggi, "Bio-Inspired Interlocking Micro-Patterning for Tunable, Switchable and Selective Adhesion in Wet and Dusty Environments," *Small* 21 (2025): 2410527.

63. R. Herbert, J. H. Kim, Y. S. Kim, H. M. Lee, and W. H. Yeo, "Soft Material-Enabled, Flexible Hybrid Electronics for Medicine, Healthcare, and Human-Machine Interfaces," *Materials* 11 (2018): 187.

64. Z. Zhang, R. K. He, Y. X. Ding, B. Han, H. S. Wang, and Z. C. Ma, "Switchable Adhesion Interfaces: From General Mechanisms to Interfacial Design Strategies," *Advanced Materials Interfaces* 11 (2024): 2400006.

65. H. Qin, X. Y. Peng, T. H. Sui, P. Yi, and J. Li, "Adhesion Performance of Magnetically Responsive Surfaces under Wet Conditions," *Soft Matter* 20 (2024): 1943.

66. T. T. Luo, X. Q. Lu, H. Ma, et al., " Design Strategy, On-Demand Control, and Biomedical Engineering Applications of Wet Adhesion," *Langmuir* 40 (2024): 25729.

67. D. H. Kim, N. S. Lu, R. Ma, et al., "Epidermal Electronics," *Science* 333 (2011): 838.

Supporting Information

Supporting Information is available from the Wiley Online Library or from the author. **Supporting Fig. S1:** Storage modulus of the SMP (PCL:PUA=1:1) at different temperatures, with a magnified view showing the plateau in the rubbery state. **Supporting Fig. S2:** XRD patterns of SMP blends with varying PCL-to-PUA weight ratios. **Supporting Fig. S3:** Cyclic thermomechanical behavior of the SMP blend showing strain, temperature, and recovery stress over three shape memory cycles. In each cycle, the sample was stretched to a programmed strain (ε_p) above T_m, cooled under fixed strain to store the temporary shape, and then unloaded to obtain the fixed strain (ε_u) for determining the shape-fixity ratio ($R_f = \varepsilon_u / \varepsilon_p$). Upon reheating above T_m, the residual strain (ε_r) was measured to calculate the shape-recovery ratio ($R_r = (\varepsilon_u - \varepsilon_r) / \varepsilon_u$). These parameters quantify the material's ability to fix and recover a programmed shape. **Supporting Fig. S4:** Photographs displaying the *CA*s of water droplets on MSMP patches with varying spacing ratio ($SR = s/d$) and corresponding solid fraction (f_s). **Supporting Fig. S5:** Side-view images of the MSMP/water interface during the pressing process, showing stable Cassie-state water repellency and expulsion of interfacial water prior to heating. **Supporting Fig. S6:** Optical images of the MSMP microstructures in the rigid glassy state (T = 30°C) under different normal preloads (20, 50, 100, and 200 kPa). The pillars remain structurally intact up to 100 kPa, with noticeable deformation observed only at 200 kPa. **Supporting Fig. S7:** Pull-off capacity of the MSMP patch measured in the ON and OFF states under varying applied preloads. **Supporting Fig. S8: Finite-element thermal analysis of MSMP heating under submerged conditions.** a) Schematic of the simulation geometry and a cross-sectional view showing the MSMP/glass interface (red line). b) Temperature fields at water temperatures of 25°C and 10°C. c) Temperature profiles along the MSMP/glass interface for different surrounding water temperatures (25, 20, 15, and 10°C). **Supporting Fig. S9:** Pull-off capacity of the MSMP in the ON state at different water temperatures. **Supporting Fig. S10:** Pull-off capacity of the MSMP patch in the ON and OFF states, and the corresponding switching ratio, as a function of SMP weight ratio (PCL:PUA). **Supporting Fig. S11: Temperature-dependent adhesion switchability and response time of the MSMP.** a) Adhesion "ON" state. (i) Schematic sequence and representative temperature–time and stress–time curves for the ON state. (ii) Pull-off strength as a function of ON time (t_{ON}). b) Adhesion "OFF" state. (i) Schematic sequence and representative temperature–time and stress–time curve for the OFF state. (ii) Pull-off strength as a function of OFF time (t_{OFF}). **Supporting Fig. S12: Effect of substrate surface energy on wet adhesion and its repeatability.** a) Pull-off capacity of the microstructured MSMP patch and the planar SMP patch measured on three substrates with different surface energies. b) Cycle-to-cycle adhesion stability of the MSMP patch over 100 repeated measurements on the same substrates. **Supporting Fig. S13:** Pull-off capacity of the MSMP patch over 72 h under wet conditions. **Supporting Fig. S14: Repeatability and reliability of the MSMP-based gripper system.** a) Force–displacement curves of the gripper system with the MSMP during the first cycle and after 25 and 50 cycles against a ground glass. b) Success rate of grasping various objects using MSMP for 50 trials. **Supporting Fig. S15:** Pull-off capacity as a function of heating temperature for (left) surface adaptation (strong adhesion) and (right) reheating temperature for self-detachment (weak adhesion). **Supporting Table S1:** Comparison of MSMP patch and recently reported switchable wet adhesives with respect to strength in the "on" and "off" states, as well as the adhesion switching ratio.